



HAL
open science

On the Influence of Slopes, Source, Seabed and Water Column Properties on T Waves: Generation at Shore

Alexis Bottero, Paul Cristini, Dimitri Komatitsch

► **To cite this version:**

Alexis Bottero, Paul Cristini, Dimitri Komatitsch. On the Influence of Slopes, Source, Seabed and Water Column Properties on T Waves: Generation at Shore. *Pure and Applied Geophysics*, 2020, 177, pp.5695-5711. 10.1007/s00024-020-02611-z . hal-03014346

HAL Id: hal-03014346

<https://hal.science/hal-03014346>

Submitted on 16 Nov 2021

HAL is a multi-disciplinary open access archive for the deposit and dissemination of scientific research documents, whether they are published or not. The documents may come from teaching and research institutions in France or abroad, or from public or private research centers.

L'archive ouverte pluridisciplinaire **HAL**, est destinée au dépôt et à la diffusion de documents scientifiques de niveau recherche, publiés ou non, émanant des établissements d'enseignement et de recherche français ou étrangers, des laboratoires publics ou privés.

1 On the influence of slopes, source, seabed and water column
2 properties on T waves: generation at shore

3 Alexis Bottero* · Paul Cristini ·
4 Dimitri Komatitsch[†]

5

6 Received: date / Accepted: date

7 Abstract The term T waves is generally associated with acoustic waves generated
8 by seismic events that subsequently travel horizontally in the ocean at the speed
9 of sound. In this paper, we use a time-domain spectral-element method to perform
10 a parametric study of the influence of seafloor slope, source position and media
11 properties for a typical (downslope) T-wave generation scenario.

12 We find that the energy and duration of these waves are particularly sensitive
13 to the environment. In particular, the slopes and physical characteristics of the
14 seabed play a crucial role for both the generation and the conversion of these
15 waves. Likewise, the depth and position of the earthquake relative to the slope is
16 of great importance, with the presence of privileged areas for the generation of T
17 waves, which we map.

18 Keywords T waves · Ocean Acoustics · Parametric study · Full-wave numerical
19 simulation · High-performance computing

Aix Marseille Univ., CNRS, Centrale Marseille, LMA, Marseille, France.

* Corresponding author. E-mail: alexis.bottero@gmail.com

[†] Deceased January 21, 2019

20 1 Introduction

21 When a seismic event occurs near an ocean basin, part of the energy produced
22 can be channeled into the water layer and then travel horizontally in this natural
23 waveguide at the speed of sound in water. In ocean acoustics, T waves have been
24 the subject of much attention since their discovery in the 1940s (Linehan, 1940).
25 They typically have a frequency range between 1 and 100 Hz and can be generated
26 from seismic waves in two main ways: by successive reflections between the sea
27 surface and a sloping seabed (downslope conversion), or by diffraction by roughness
28 or by heterogeneities (see Okal, 2007 for a review on the topic). In this article we
29 will let aside T waves created by diffraction and focus on T waves generated by
30 downslope conversion.

31 Once channeled into the water layer, T waves can travel particularly far for
32 several reasons. First, by propagating in the ocean, they spread in an almost
33 cylindrical fashion, which causes less decay than in the case of spherical geometrical
34 spreading in free space as for P and S waves (see Fox and Dziak, 1998). Second,
35 the attenuation of acoustic waves in water is particularly low at the frequencies
36 considered. Third, due to the fact that temperature and pressure vary with depth,
37 the speed of sound waves in the ocean typically presents a minimum around 1000
38 m in the Atlantic ocean. This feature, known as the Sound Fixing and Ranging
39 (SOFAR) channel, makes it possible, under certain conditions, to facilitate energy
40 transmission. For all these reasons, T waves can therefore propagate over very
41 large distances, in practice only limited by the size of ocean basins (see Okal and
42 Talandier, 1997; Metz et al., 2016 for example). Even a moderate seismic event can
43 be detected thousands of kilometers away if it has generated T waves. Thus, the
44 event detection threshold can be improved by one to two orders of magnitude using
45 only a handful of instruments located either at sea (hydrophones or OBS), or in
46 the immediate vicinity of the shore (T-phase stations) rather than large terrestrial
47 seismic networks (Johnson and Northrop, 1966; Fox et al., 1994; De Groot-Hedlin
48 et al., 2004; Pan and Dziewonski, 2005; Dziak et al., 2011). Nevertheless, it should

49 be noted that instruments at sea may pose other problems related, for instance,
50 to their location or to the transmission of recorded data.

51 After their oceanic path, T waves may reach the coasts. Upon arrival on the
52 continental slope, they convert back into seismic waves that can be detected by
53 inland seismometers. Since acoustic waves travel more slowly in water than in the
54 ground, converted T-waves typically arrive after longitudinal waves (P waves, also
55 called primary) and shear waves (S waves, also called secondary), hence their name
56 "T" as tertiary (Linehan, 1940).

57 However in many cases, such as small seismic events along mid-ocean spreading
58 ridges, only T waves are detected. They are the only available piece of information
59 on these events (see for example Fox et al., 1994). T waves are therefore used
60 in many fields of geosciences. Since the 1960s, thousands of T waves have been
61 recorded and used for earthquake location (see Johnson, 1966; Duennebier and
62 Johnson, 1967; Fox et al., 2001) and algorithms now exist for their automatic
63 recognition (Sukhovich et al., 2014). Although the location of the conversion zone is
64 sometimes difficult, these measurements have made it possible to identify volcanic
65 eruptions (Dietz and Sheehy, 1954; Norris and Johnson, 1969; Talandier and Okal,
66 1987; Schreiner et al., 1995; Fox and Dziak, 1998; Bohnenstiehl et al., 2013) or to
67 monitor eruptive processes in real time (Fox et al., 1995; Dziak et al., 2011).
68 These detections contributed greatly to our understanding of hydrothermal and
69 microbial processes in ocean ridges (Delaney et al., 1998; Cowen et al., 2004;
70 Wilcock et al., 2014). T waves are also very useful for detecting small intra-plate
71 earthquakes in very remote regions (Fox et al., 2001) and for studying seafloor
72 expansion or magma intrusion at ocean spreading ridges (Hammond and Walker,
73 1991; Fox et al., 1994; Schreiner et al., 1995; Blackman et al., 2000) that affect
74 the ocean and marine ecosystems (Dziak et al., 2011, 2012). Although not caused
75 by "earthquakes", it is interesting to note here that collisions between icebergs
76 can also generate similar hydroacoustic signals (see e.g. Talandier et al., 2006;
77 Matsumoto et al., 2014).

78 For large earthquakes in oceanic regions, T waves can also be used together with
79 P and S waves to map the different components of the fault rupture (see Graeber
80 and Piserchia, 2004; De Groot-Hedlin, 2005; Guilbert et al., 2005; Tolstoy and
81 Bohnenstiehl, 2005, 2006). Moreover, some links between T waves and tsunamis
82 have now been established and could potentially be used in a warning system
83 (Ewing et al., 1952; Tolstoy and Bohnenstiehl, 2006; Salzberg, 2008). In addition,
84 T waves can also provide information on the earthquake that generated them
85 (Dziak, 2001; Talandier and Okal, 2016), on the surface seismic characteristics of
86 coastal regions (Koyanagi et al., 1995; Kosuga, 2011) or on the deep structure of
87 the Wadati-Benioff zone (Okal, 2001). It is expected that T waves may also be
88 used to study mesoscale variations of the ocean properties (Evers and Snellen,
89 2015).

90 Finally, acoustic signals recorded in the oceans have been used for several
91 years to distinguish between anthropogenic and natural sources such as nuclear
92 explosions and volcanoes, in particular under the Comprehensive Nuclear-Test-
93 Ban Treaty (CTBT) adopted by the United Nations General Assembly in 1996
94 (see De Groot-Hedlin and Orcutt, 1999, 2001)). Indeed, the strong compressional
95 waves generated by explosions can sometimes convert into acoustic wave traveling
96 in the ocean which may then be detected at far distance hydroacoustically, but
97 not seismically (see Adams, 1979).

98 At the interface between seismology and underwater acoustics, the T-wave
99 phenomenon involves complex and diverse processes whose mechanisms are often
100 poorly understood, which limits the possibilities for in-depth theoretical analysis.
101 These processes include viscoelasticity, seismic-to-acoustic and acoustic-to-seismic
102 conversion, slopes, diffraction, guided propagation in the ocean, high frequencies,
103 3-D effects, or complex geometries. In this context, it is still difficult to correctly
104 assess the influence of the characteristics of the earthquake, the seabed or the
105 ocean, for example. These issues are still open nowadays. In particular, they limit
106 the correct assessment of earthquakes epicenters from T waves (see Williams et al.,

2006; Chapman and Marrett, 2006; Lecoulant et al., 2019). In particular, slopes have long been known to play a crucial role on both T-wave generation (e.g. Wadati and Inouye, 1953; Shurbet, 1955; Shurbet and Ewing, 1957; Johnson et al., 1963 ...) and conversion (e.g. Tolstoy and Ewing, 1950; B ath, 1954 ...) at shore, but their influence has not been quantified.

In this context, as in many other research areas, numerical simulation seems to be an appropriate approach for the study of T waves. Numerical modeling has long been used in ocean acoustics (Jensen et al., 2011), for instance based on finite elements or on parabolic equation solvers. In recent years a time-domain Spectral Element Method (SEM, Komatitsch and Tromp, 1999) has also been used successfully in the field of underwater acoustics (Cristini and Komatitsch, 2012; Jamet et al., 2013; Bottero et al., 2016; Lecoulant et al., 2019). Beyond its capability of handling complex geometries and rheologies accurately, as any finite-element technique, the time-domain spectral-element method runs efficiently on very large computers, thus providing a drastic reduction of the duration of numerical simulations, which is one of its attractive properties.

This article presents a parametric study, based on such a SEM, of the influence of seafloor slope, source position and media properties for a typical (downslope) T-wave generation scenario. The article is organized as follows: in Section 2 we describe the numerical method we use to generate the numerical results. Section 3 and 4 are then devoted to the study of the influence of slope angle on the energy of the transmitted T wave. In Section 5 we present some results concerning the influence of earthquake location on T-wave energy and duration. Some conclusions and perspective are drawn in Section 6.

2 The spectral-element method for ocean acoustics

The SEM is one of the most efficient numerical methods for performing numerical simulations in the time domain for the solution of the full-wave equation. In this section, we recall the main characteristics of the SEM and we focus only on some

135 of its most important features. The reader is referred to the chapter 4 of reference
136 Fichtner (2010) for more details on the method and to reference Peter et al. (2011)
137 for a review of its capabilities for both forward and inverse modeling. The SEM is
138 based upon a high-order piecewise polynomial approximation of the weak formula-
139 tion of the wave equation. It combines the accuracy of the pseudospectral method
140 with the flexibility of the finite-element method. In this method, the wavefield is
141 represented in terms of high-degree Lagrange interpolants, and integrals are com-
142 puted based upon Gauss-Lobatto-Legendre quadrature. This combination leads
143 to a perfectly diagonal mass matrix, which in turn leads to a fully explicit time
144 scheme that lends itself very well to numerical simulations on parallel computers.
145 It is particularly well suited to handling complex geometries and interface condi-
146 tions. The use of a pseudospectral method also allows for the use of coarser meshes
147 compared to classical finite-element methods. Very distorted mesh elements can
148 be accurately handled and complex models that include fluid, elastic, viscoelastic,
149 anisotropic or porous media can be modeled, making the SEM a method of choice
150 for the numerical modeling of wave propagation through various types of media
151 encountered in ocean acoustics. This numerical method has been thoroughly val-
152 idated with analytical codes and is used by many researchers in seismology all
153 over the world . Additionally, Convolutional Perfectly Matched Layers (CPML)
154 are used to remove spurious reflections from the boundaries of the computational
155 domain (Komatitsch and Martin, 2007; Xie et al., 2016). Finally, the SEM is well-
156 suited for parallel implementations on supercomputers as well as on clusters of
157 GPU cards by using the Message-Passing Interface (MPI) library and overlapping
158 communications with calculations to hide their cost. This is an important feature
159 for high-performance computing which is absolutely necessary for the configura-
160 tions we are considering in the present paper. For the mesh generation, we used
161 the meshing software Trelis (developed by Sandia National Laboratories, USA).

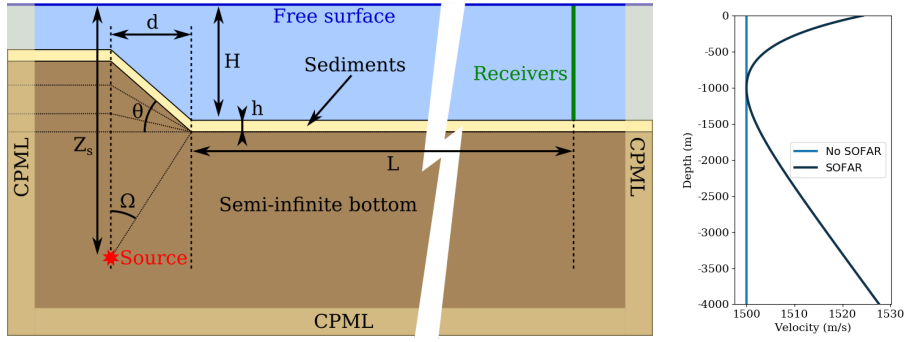


Fig. 1 Left: Setting of the study. The objective is to analyze the influence of slope angle θ and sediment properties on T-wave energy transmitted at the green receiver line situated at range $L + d = 85$ km. The geometry is 2-D Cartesian. The source is located at depth $Z_s = 30$ km, the sediments are $h = 0.4$ km thick, the abyssal plain is located at depth $H = 4$ km, and the slope has a horizontal length of $d = 5$ km. The angle Ω is fixed at 11.05 degrees. The receiver line is at $L = 80$ km from the bottom of the slope. In the spectral-element simulations the energy that reaches the edges of the model is absorbed by CPML (see text; Xie et al., 2016) absorbing layers. Right: Sound speed profiles in the sea used in the numerical simulations. The curve labeled "SOFAR" refers to a classical idealized ocean sound-speed profile (Munk, 1974) with minimum velocity at a depth of 1000 m.

162 3 Common characteristics of T-wave downslope conversion, parametric study

163 Research on T waves in the late 1950s and the beginning of the 1960s had indi-
 164 cated that continental slopes were probably instrumental in the generation of T
 165 phases (e.g. Tolstoy and Ewing, 1950; Ewing et al., 1952). However, it is in the
 166 paper of Johnson et al. (1963) that the first detailed explanation of the generation
 167 mechanism of T waves generated by non-surficial earthquakes can be found. This
 168 article suggests that seismic energy may be trapped into the SOFAR channel after
 169 successive reflections between a downsloping seafloor and the sea surface, making
 170 it travel horizontally. This scenario, which they call downslope conversion, is based
 171 on ray tracing. T-wave amplitude is known to strongly depend on bathymetry (see
 172 e.g. Williams et al., 2006; Chapman and Marrett, 2006). This has been recently
 173 confirmed by Lecoulant et al. (2019).

174 We will first study the influence of slopes, seabed and water column properties
 175 on T-wave energy received at a receiver line for a typical downslope conversion
 176 scenario (Figure 1).

177 This 2D Cartesian model consists of a homogeneous elastic semi-infinite bottom
178 overlain by a 400 m-thick homogeneous elastic sedimentary layer. The seafloor has
179 a constant slope with a horizontal extension of $d = 5$ km. The seismic source is
180 placed right below its upper end. Contrary to a similar study carried out by Frank
181 et al. (2015), we have chosen to keep the horizontal length of the slope constant
182 in order to keep the solid angle from which the source sees the slope unchanged
183 (denoted by Ω in the figure).

184 It is important to note here that although a 2-D Cartesian model of the slope
185 seems to be perfectly adequate for this study, the source in this model is physically
186 an infinite line source. With this in mind, it may seem better to work using cylin-
187 drical coordinates assuming axisymmetry rather than 2-D Cartesian coordinates.
188 However, one would then observe multiply-reflected energy between the highest
189 slopes and the symmetry axis that do not exist in reality¹. However, fortunately,
190 the use of 2D Cartesian coordinates rather than cylindrical coordinates is not crit-
191 ical for this qualitative study. It should be noted here that of course a 3-D model
192 would be the most appropriate. Unfortunately, the number of wavelengths in the
193 model currently makes this study impractical with "reasonable" computational
194 resources. We believe, however, that the approximation is justified and that the
195 results obtained would not be substantially different if considering a 3-D model.
196 The source is placed on the downward oriented z-axis. We chose to carry the study
197 for a shallow seismic source located in the elastic part at $Z_s = 30$ km below the
198 sea surface. The receiver line is located at range 85 km.

199 We consider four different sediment types, labeled LOW, MED, HIGH and
200 "HIGH, with low density" respectively for low, medium and high velocity contrast
201 between the crust and the water. Their properties are given in Table 1. Note that
202 the properties labeled HIGH match the semi-infinite bottom properties, which
203 means that there is no sedimentary layer. Note also that the case "HIGH, with

¹ This could happen, though, in the case of an earthquake occurring right below a volcano or a seamount, but we are not interested in these specific cases here

Table 1 Properties of the semi-infinite bottom and of the four types of sediments used. ρ is the density, V_p is the compressional wave speed, V_s is the shear wave speed, and α_p and α_s are the corresponding attenuation coefficients expressed in dB per wavelength.

Label used	Description
Semi-infinite bottom	$\rho = 2500 \text{ kg.m}^{-3}$, $V_p = 5500 \text{ m.s}^{-1}$, $V_s = 3235 \text{ m.s}^{-1}$ $\alpha_p = 0.17 \text{ dB}.\lambda_p^{-1}$, $\alpha_s = 0.17 \text{ dB}.\lambda_s^{-1}$
HIGH	$\rho = 2500 \text{ kg.m}^{-3}$, $V_p = 5500 \text{ m.s}^{-1}$, $V_s = 3235 \text{ m.s}^{-1}$ $\alpha_p = 0.17 \text{ dB}.\lambda_p^{-1}$, $\alpha_s = 0.17 \text{ dB}.\lambda_s^{-1}$
MED	$\rho = 2200 \text{ kg.m}^{-3}$, $V_p = 3500 \text{ m.s}^{-1}$, $V_s = 2060 \text{ m.s}^{-1}$ $\alpha_p = 0.46 \text{ dB}.\lambda_p^{-1}$, $\alpha_s = 0.46 \text{ dB}.\lambda_s^{-1}$
LOW	$\rho = 2200 \text{ kg.m}^{-3}$, $V_p = 2000 \text{ m.s}^{-1}$, $V_s = 1000 \text{ m.s}^{-1}$ $\alpha_p = 0.46 \text{ dB}.\lambda_p^{-1}$, $\alpha_s = 0.46 \text{ dB}.\lambda_s^{-1}$
HIGH, with low density	$\rho = 2200 \text{ kg.m}^{-3}$, $V_p = 5500 \text{ m.s}^{-1}$, $V_s = 3235 \text{ m.s}^{-1}$ $\alpha_p = 0.17 \text{ dB}.\lambda_p^{-1}$, $\alpha_s = 0.17 \text{ dB}.\lambda_s^{-1}$

low density" is meant to highlight the effect of a variation in density only (in comparison with case HIGH).

Let us also emphasize that in this configuration, the sedimentary layer covers the whole seafloor and not only the slope. It therefore has an influence on energy transmission, not only for the T-wave conversion but also all along the propagation in the water layer. This will have to be kept in mind when comparing the results obtained with different sedimentary layers.

In the water layer, the density is equal to 1000 kg.m^{-3} and the sound velocity is either a constant velocity of 1500 m.s^{-1} or a classical ocean sound-speed profile (Munk, 1974, see Figure 1, right). At the distance and frequencies considered the sound attenuation in the water is considered negligible (see Jensen et al., 2011).

Several numerical simulations were performed using the time-domain spectral-element method mentioned above. The source is a vertical force; its source time function is a Ricker wavelet (second derivative of a Gaussian) with a dominant frequency $f_0 = 4 \text{ Hz}$. The wave field is computed up to a range of 110 km and down to a depth of 35 km, the energy coming out of this box (shown in Figure 1) being absorbed by perfectly matched absorbing boundary layers. For each slope angle between 0 and 34° (with an increment of one degree), eight simulations are performed, one for each of the four types of sediments in Table 1 for either a

223 constant sound speed in the water or a sound speed profile (Figure 1, right). Let
 224 us point out here that the maximum slope angle considered (34°) is related to the
 225 choice that has been made of preserving a constant horizontal length d for the
 226 slope (see Figure 1, left). Beyond this value the slope can cross the sea surface.

227 Each mesh is composed of ~ 0.12 million spectral elements whose polynomial
 228 degree is $N = 4$. The total number of unique Gauss Lobatto Legendre points GLL
 229 in the mesh is approximately 2 million. In the worst case for all these meshes, 99.9%
 230 of the acoustic elements ensure a sampling of the signals of at least 5 grid points
 231 per pressure wavelength in the fluid, and 99.9% of elements in the viscoelastic
 232 part ensures at least 6.5 points per shear wavelength, thus accurately sampling
 233 the wave field up to frequencies of ~ 10 Hz. We select a time step $\Delta t = 0.72$ ms
 234 for the explicit, conditionally-stable Newmark time scheme, and simulate a total
 235 of 0.2 million time steps, i.e. 140.0 s. The displacement is recorded at the receiver
 236 line shown in Figure 1, which comprises 20 evenly-spaced receivers. All simulations
 237 ran simultaneously on 10,080 processor cores of a supercomputer. The whole run
 238 lasted approximately 2 hours. An example of the time signal corresponding to the
 239 (horizontal) particle velocity generated in the middle of the receiver line for the
 240 case labeled HIGH, with a SOFAR channel and with a slope of $\theta = 20^\circ$ is shown
 241 in the right-hand side in Figure 2, together with the same signal but calculated
 with 0° slope (left-hand side).

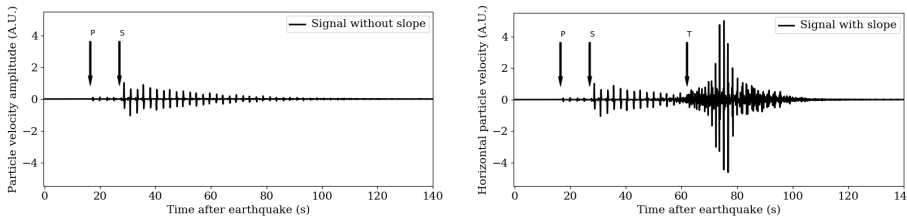


Fig. 2 Synthetic horizontal particle velocity recorded at a receiver located in the middle of the receiver line (see Figure 1) for the case labeled HIGH, with a SOFAR channel. Left: case with a reference slope of $\theta = 0^\circ$. Right: case with a slope of $\theta = 20^\circ$. For time < 50 s the two signals are almost identical and thus, in order to remove the body waves and to keep only the T wave, the signal on the left (corresponding to the reference slope of $\theta = 0^\circ$) is subtracted from the signal on the right generated with a non-zero slope. Vertical particle velocity is similar.

243 Arrivals from the P and S waves are clearly visible in both time series (they are
 244 almost identical below 40 s) and do not depend on the slope. The T phase appears
 245 only in the presence of the slope, as expected. In order to remove the body waves,
 246 the reference signal for a flat bottom is subtracted from the signal generated with
 247 a slope bottom. Such processing is of course not fully satisfactory, as the signals
 248 obtained may also contain energy from other phenomena than T waves that may
 249 overlap with it. Nevertheless such superposition is unlikely and we suppose that
 250 it does not occur in our configurations.

251 4 Transmitted energy as a function of slope angle

252 Let us denote $u_1(\mathbf{x}, t)$ and $u_2(\mathbf{x}, t)$ the horizontal and vertical T phase displacement
 253 fields and $P(\mathbf{x}, t)$ the T-phase pressure field at time t and position $\mathbf{x} = (x, z)$,
 254 obtained after subtraction of the reference signals. $\dot{u}(\mathbf{x}, t) = \sqrt{\dot{u}_1(\mathbf{x}, t)^2 + \dot{u}_2(\mathbf{x}, t)^2}$
 255 is the norm of the particle velocity of the T phase. The field that represents the
 256 instantaneous T-wave energy per unit volume in the fluid is given by (Jensen et al.,
 257 2011 pp.11-12):

$$\mathcal{E}(\mathbf{x}, t) = \frac{1}{2}\rho\dot{u}^2(\mathbf{x}, t) + \frac{1}{2}\frac{P^2(\mathbf{x}, t)}{\rho(\mathbf{x})c^2(\mathbf{x})}, \quad (1)$$

258 where ρ is the density of water and $c(\mathbf{x})$ is the distribution of sound velocity.
 259 Let T_f refer to the final time of the simulation; we can then define the integrated
 260 T-wave energy field by:

$$E(\mathbf{x}) = \int_0^{T_f} \mathcal{E}(\mathbf{x}, t) dt. \quad (2)$$

261 This quantity is similar to the radiated seismic energy introduced by Boatwright
 262 and Choy (1986) and evaluated from body wave measurements. It can also be seen
 263 as a generalization of the T-Phase Energy Flux (TPEF) proposed by Okal (2003)
 264 to characterize the part of the energy generated by an earthquake source which is
 265 converted into a T wave. This approach was used in Bottero et al. (2018) to com-

266 pute broadband transmission loss maps from numerical simulations in the time
 267 domain.

268 Integrating E over depth along the receiver line (situated at range $L + d$, see
 269 Figure 1) gives an averaged transmitted energy in the water layer:

$$\langle E \rangle = \frac{1}{H} \int_{-H}^0 E(L + d, z) dz \quad (3)$$

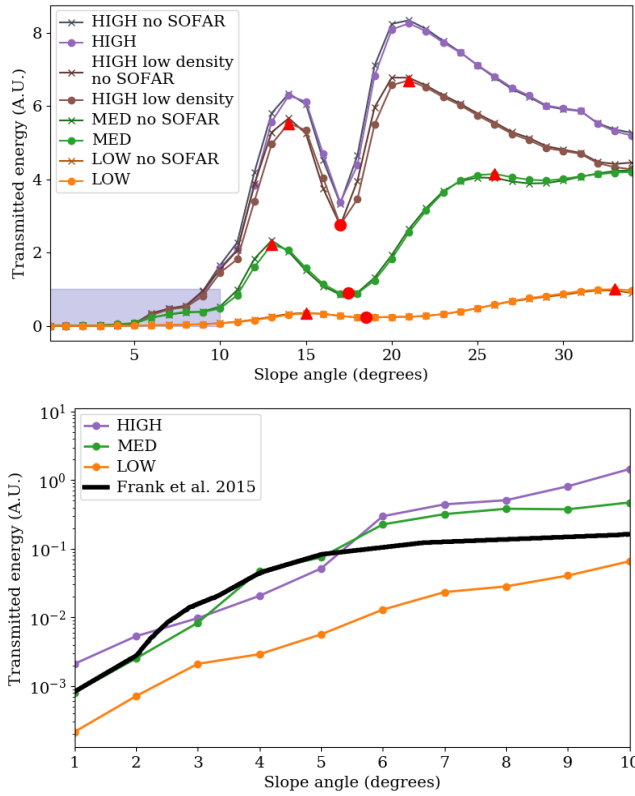


Fig. 3 Top: Transmitted T-wave energy at 85 km as a function of slope angle for four different sediments of Table 1 and for two different sound speed profiles in the ocean (Figure 1, right). The red triangles indicate the local maxima, and the red circle indicates the position of the trough. The blue shaded box represents the area studied by Frank et al. (2015). Bottom: Zoom on the blue shaded area of the left picture, showing also a comparison in logarithmic scale between our results and the curve shown in Frank et al. (2015) (re-scaled).

270 We compute the quantity $\langle E \rangle$ as a function of the slope angle for the four dif-
 271 ferent sediment types (described in Table 1) and the two different velocity profiles

272 in the ocean (shown in Figure 1, right). The result is shown in Figure 3 (top). The
273 curves have a typical shape exhibiting two maxima (marked with red triangles in
274 the figure) and a trough in between. Let us first remark that the SOFAR channel
275 does not seem to have a significant influence on the results at this range. It can also
276 be seen that low sediment densities penalize energy transmission without affecting
277 the global shape of the transmission curves, as expected from Snell’s law.

278 The particular shape of these curves can be physically explained by considering
279 the (quasi-)plane wave reflection/transmission energy coefficients of the interfaces
280 considered. These coefficients are shown in Figures 4 and 5 as the function of the
281 incidence angle with respect to the normal to the surface. They were obtained
282 numerically from parametric simulations (see Rosenkrantz et al., 2019). These
283 coefficients take into account the two viscoelastic crustal interfaces: the transmis-
284 sion between the semi-infinite bottom and the different sediment configurations
285 given in Table 1 and the reflection between the water medium (here considered as
286 semi-infinite) and the sediments. The setting used to calculate these coefficients is
287 illustrated in Figures 4 and 5. It should be noted here that for the transmission
288 coefficient from the viscoelastic half-space to the water half-space the plane wave
289 is a plane force source (thus composed of compressional and shear wave) whose
290 direction of excitation corresponds to the direction of propagation of the plane
291 wave. This ensures that the compressional to shear wave energy ratio in the in-
292 cident plane wave is consistent with the setting considered in Figure 3 where a
293 vertical point force has been used.

294 At this point, it is important to emphasize that attenuation, in particular, plays
295 a very important role in energy reflection at the fluid/viscoelastic solid interfaces
296 (see e.g. Carcione and Helle, 2004). This is particularly clear in Figure 5 at the
297 top left of the middle sub-figure, for the HIGH case which shall be taken as an
298 illustration here (even if it is actually the least attenuating case). The low-reflection
299 band (high-transmission) around 30° corresponds to the Rayleigh angle. At this
300 incidence a large part of the energy is converted into surface waves (Stoneley-

301 Scholte waves) that propagate along the interface. If the attenuation is neglected,
 302 the reflection is total for this incidence angle. The trough becomes larger as the
 303 attenuation increases.

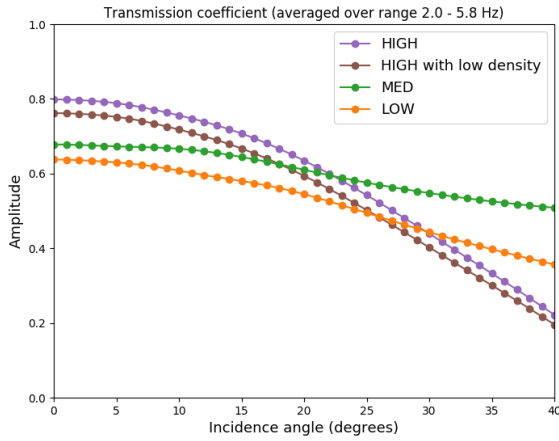
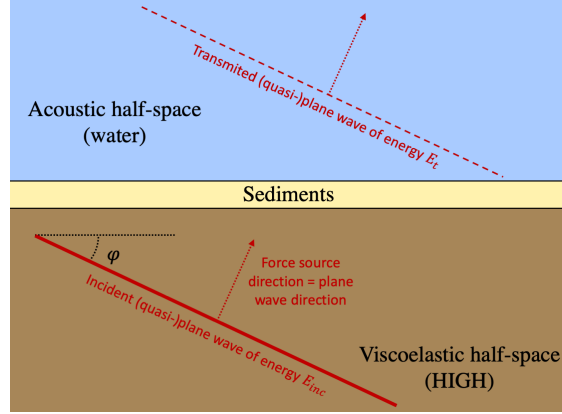


Fig. 4 Top: setting of the energy transmission coefficient shown below (E_{inc}/E_t). Bottom: semi-infinite bottom to sediments to water energy transmission coefficient as a function of the incidence angle φ (defined in the top sub-figure) for the cases described in Table 1. These values have been averaged over the bandwidth of the source.

304 It should also be noted that the presence of a sediment layer results in a
 305 reflection coefficient that depends on frequency (see HIGH with low density, LOW
 306 and MED cases in the top of the middle sub-figure in Figure 5). To make it
 307 easier to interpret the results, the average of the coefficients around 4 Hz will be

308 considered, which corresponds to the dominant frequency of the source. The curves
309 are shown in the bottom of Figure 5. For the sake of conciseness, and because they
310 are not varying much, only these averaged curves are shown for the transmission
311 coefficient.

312 From these curves and geometrical ray consideration one can then attempt to
313 interpret Figure 3. From a zero slope to about 10° , when the slope increases, the
314 amount of energy transmitted into the water column varies only slightly because
315 the transmission coefficient is almost constant.

316 On the other hand, the number of reflections undergone by the wavefronts be-
317 fore reaching the receiver line decreases, which tends to favor better transmission.
318 This effect is dominant compared to the variation in the reflection coefficient for
319 subsequent reflections on the seabed.

320 For slopes from 10° to about 18° the same phenomenon continues but now the
321 role of the reflection coefficient gets more important. At this range the wavefronts
322 reaching the receivers (after one or several reflections on the slope) steepen from
323 approximately 15° to 30° . This corresponds to a sharp increase in reflection coef-
324 ficient followed by a trough corresponding to the generation of surface waves (see
325 Figure 5). This is particularly true in the cases MED and HIGH². At the same
326 time, the proportion of energy that reaches the slope and that is reflected, at least
327 once on it, decreases. This results in a less horizontal propagation subsequently
328 and thus in more reflections to reach the receivers.

329 These two phenomena both explain the first maximum and the following trough.

330 When the slope further steepens (above about 18°), the incidence angles (rela-
331 tive to the vertical) of the wavefronts in the water column further increase and get
332 above about 30° . These values are associated with a sharp growth of the reflection
333 coefficient at the seafloor. This strong effect prevails over all the others and ex-
334 plains the second step rise of the downslope converted T-wave transmission with
335 slope. After this angle the transmitted energy is only governed by the seabed to

² In the case MED the reflection peak mentionned is around 22° while in the case HIGH it is around 27° (see Figure 5, bottom)

336 water transmission coefficient, which decreases slowly, and by the reflection coef-
 337 ficient for incidence angles above 35° , which is constant in the case HIGH and
 338 fluctuates in the cases MED and LOW. These effects explain the presence of the
 339 second maximum in the curves in Figure 3.

340 When decreasing the impedance contrast between the water and the sediments
 341 (going from HIGH to LOW), the overall shape of the curve is preserved but is
 342 damped because of the lower average reflection coefficients.

343 The shift towards the higher slope angles when decreasing the impedance con-
 344 trast is explained by the refraction of the incident wave at the seabed. The softer
 345 the sediments, the more vertically the energy spreads once in the water.

346 Figure 3 (bottom) shows a comparison of our numerical results with those of
 347 Frank et al. (2015) obtained, for small slopes, based on a parabolic equation solver.
 348 Let us mention that significant differences exist between the setting of their nu-
 349 merical model and ours: they used an axisymmetric geometry³, they considered
 350 a homogeneous seafloor, similar to our case labeled MED but with a lower atten-
 351 uation of $\alpha_p = 0.05 \text{ dB} \cdot \lambda_p^{-1}$, $\alpha_s = 0.10 \text{ dB} \cdot \lambda_s^{-1}$, a 5 Hz monochromatic source
 352 located at $Z_s = 10 \text{ km}$ (instead of a broadband source with dominant frequency
 353 4 Hz at $Z_s = 30 \text{ km}$ in our case), a receiver line at range 150 km (instead of 85
 354 km) and, more importantly, a different way of parameterizing the slope variations.
 355 In their model, the depth of the top of the slope is fixed and the horizontal ex-
 356 tent of the slope consequently changes for each slope angle. This implies that the
 357 solid angle (labeled Ω in Figure 1) varies for each slope, thus favoring the lowest
 358 slopes (which receive more energy) compared to steepest ones. In our opinion,
 359 this is the main reason for the slight differences observed between the results of
 360 the two models. Nevertheless, Frank et al. (2015) reached the same conclusion
 361 in the slope range 0° to 10° : there is a smooth increase of transmitted energy
 362 with increasing slope angle. We have seen in this section that steeper continental

³ As the parabolic equation does not take into account back-scattered energy, they do not face the problem of multiple reflections between the slope and the symmetry axis that we mentioned and that prevented us from using axisymmetric calculations in our case.

363 slopes actually involve more complicated physical phenomena than gentle slopes.
 364 However, steep slopes are frequently encountered at atolls (Talandier and Okal,
 365 1998) or at seamounts and ridges (see e.g. Chapman and Marrett, 2006). It is also
 366 worth mentioning that, in our study, the differences estimated in energy transmis-
 367 sion between a hard (such as our case labeled HIGH for example) gently-dipping
 368 seabed (say a 5° slope) and a steeper one (14°) can reach a factor of 100, which
 369 could bias localization techniques towards steep slopes. This was already observed
 370 and documented in the literature (Northrop, 1962; De Groot-Hedlin and Orcutt,
 371 2000), although not quantified to our knowledge. It is interesting to note that the
 372 opposite situation is also possible. Indeed, differences in energy transmission be-
 373 tween an optimally-dipping area (i.e. a slope of 14° for our case labeled HIGH for
 374 example) and a steeper slope but located in the transmission trough (17°) may
 375 bias the estimated source locations towards the lowest slopes.

376 5 Influence of source position on T-wave energy and duration

377 T-wave amplitude and duration are known to strongly vary depending on the
 378 position of the source with respect to the bathymetry (see e.g. Williams et al.,
 379 2006; Lecoulant et al., 2019). In this section this particular aspect will be investi-
 380 gated within an energy-based framework. Let us first define T-wave duration for
 381 this study. Energy and duration are two quantities of equal importance because
 382 a large energy distributed over a long period of time can go unnoticed in the
 383 presence of noise, and conversely, a limited but concentrated energy over a short
 384 period is generally more visible. In equations (1), (2) and (3) we have defined the
 385 instantaneous T-wave energy $\mathcal{E}(\mathbf{x}, t)$, the integrated T-wave energy $E(\mathbf{x})$ and the
 386 averaged transmitted T-wave energy $\langle E \rangle$, whose computation has been detailed
 387 above. One can also define the maximum T-wave energy field:

$$M(\mathbf{x}) = \max_{t < T_f} \mathcal{E}(\mathbf{x}, t). \quad (4)$$

388 where T_f is the physical duration of the simulation. It gives the maximum instan-
 389 taneous energy at each point and provides a way of defining an "effective" T-wave
 390 duration field as:

$$\mathcal{T}(\mathbf{x}) = 2 \frac{E(\mathbf{x})}{M(\mathbf{x})}. \quad (5)$$

391 This quantity has the dimension of a duration, which is formally the duration
 392 of a signal considered as triangular⁴. Computing this field gives information on
 393 the temporal and spatial structure of the arrivals, keeping track of their spreading
 394 over time at any point of the model. As for the integrated energy, we can then
 395 define an averaged transmitted T-wave duration in the water layer:

$$\langle \mathcal{T} \rangle = \frac{1}{H} \int_{-H}^0 \mathcal{T}(L + d, z) dz, \quad (6)$$

396 which is the average effective duration of the T waves generated by the earthquake
 397 considered and recorded at a horizontal distance $L + d$ from the top of the slope.
 398 This approach is also used in Bottero et al. (2018) to calculate time dispersion
 399 maps from numerical simulations in the time domain.

400 We recall that the source we used in all our numerical simulations is a vertical
 401 force whose radiation pattern may influence the energy distribution. Nevertheless,
 402 as a first step, we chose to keep this simple source model for all numerical simula-
 403 tions. The study of the influence of the source radiation pattern will be considered
 404 in future studies.

405 To illustrate the importance of the source position on the T-wave structure, we
 406 have computed the averaged transmitted T-wave energy $\langle E \rangle$ and duration $\langle \mathcal{T} \rangle$ for
 407 351 source positions (324 being below the seafloor level). Contrary to the previous
 408 sections, the slope does not vary and is set to 20° . The medium properties are
 409 those of the case labeled MED in Table 1 and we consider a sound speed profile
 410 in the water layer. Before computing the instantaneous T-wave energy $\mathcal{E}(\mathbf{x}, t)$, the
 411 body waves have to be subtracted from the signals. For this purpose, a reference

⁴ In the case of triangular signals this effective duration is equal to their actual duration.

412 run with a flat bottom is performed for each of the 324 sources below the seafloor.
413 For the sources situated above the ocean floor no subtraction is needed, only T
414 waves are created in this case. For the sources situated below the ocean depth the
415 horizontal and vertical displacement in the cases with and without the slope are
416 subtracted point to point for all time and positions (see Figure 2 for an example
417 of such signals) before computing the instantaneous energy (1) needed for the
418 averaged energy (3) and duration (6). This subtraction procedure is not perfect
419 for the sources situated on the left side of the slope at all depths. Especially for
420 those located at the shallowest depths and at the greatest horizontal distances from
421 the slope. In these cases a significant amount of the body wave energy reaching
422 the receiver line will be different between the flat reference and the sloping model,
423 which may result in a miscalculation of the T-wave energy. That is why the results
424 will be later compared with and without subtraction.

425 The simulations were run simultaneously on 8,100 processor cores and lasted
426 approximately one hour. The results are summarized in Figure 6.

427 The first, and probably the most important, point that can be made here is
428 that these maps are not homogeneous: there are large variations in energy and
429 duration between T phases generated by sources located at different positions
430 with respect to the slope. The patterns produced are complex. We shall attempt
431 below to interpret them.

432 In the vicinity of the interface between the ocean and the seafloor some artifacts
433 can be observed. They are explained by the fact that the body waves generated
434 with and without a slope are not strictly identical anymore for these very shallow
435 source positions. For that reason, we will also compare the energies and durations
436 without subtraction (i.e. including the body waves).

437 Let us first discuss the differences between the quantities computed from the
438 full signal and those computed from the subtracted signals assumed to represent
439 T waves only.

440 Apart from the artifact, explained above, at the third line of sources the images
441 are very similar, which means that, in most cases, body waves do not influence
442 the results much. Consequently, the right -or the left- hand side of Figure 6 can
443 be used for analysis.

444 The region right below the bottom of the slope and the outset of the abyssal
445 plain are however exceptions to note. The results computed in this area show that
446 T waves can be generated, by downslope conversion, from earthquakes located
447 beneath the abyssal plain but only above a certain depth, contrary to body waves
448 that can be generated at any depth. It seems that this depth increases with the
449 distance to the slope, although this has to be confirmed by calculations over a
450 wider area. This phenomenon could have interesting implications and explain some
451 frequent outliers to the rule "epicenters at the lower end, and [...] seaward, of the
452 continental slope are typically weak or not received" (Johnson et al., 1967) even
453 without considering scattering phenomena. Example of such a signal is shown in
454 Figure 7 (bottom) it has been recorded at range $L + d$ in the middle of the water
455 layer from a source located at the red triangle shown on Figure 6.

456 It can also be noted that earthquakes that occur in the immediate vicinity of
457 the slope are particularly prone to generate strong and impulsive (short duration)
458 T waves. This result was of course expected because in that area an important part
459 of the source energy reaches the slope and thus geometrical spreading is minimum.
460 Besides, the angular sector under which the source sees the slope is maximum
461 there. Looking into more details, we can see that the energy and duration maps
462 have an interesting pattern: some regions are favored for T-wave generation and
463 exhibit high energies and short durations.

464 Let us first note that, in the case considered, both P and S wave speeds in the
465 Earth's crust (sediment and semi-infinite bottom) are greater than the sound speed
466 in the ocean. Consequently, Snell's law implies that no energy can propagate in
467 the ocean horizontally directly by refraction, which means that, even for sources in

468 favored areas, energy transmission implies at least two reflections⁵. Our numerical
469 simulations suggest that three source regions favor T-wave generation:

- 470 – The first region is situated approximately along the line starting at the top, or
471 at the middle, of the slope and tilted by an angle of 45° with respect to the
472 vertical (dashed line in Figure 6), that is to say when the epicentral distance
473 to the continental slope and the depth of the hypocenter are approximately
474 the same. This region corresponds to a tradeoff between the amount of energy
475 reflected on the slope and thus redirected towards the ocean and the grazing
476 angles (angle with respect to the horizontal direction) of the redirected signals.
477 Above that region the energy reflected on the slope is lower but has a smaller
478 grazing angle, while below that region more energy is reflected but has larger
479 grazing angle thereafter. The vicinity of the normal to the slope corresponds
480 to the area where the solid angle from which the source sees the slope is max-
481 imum. This favored region has long been known empirically (Bâth, 1954) and
482 an interpretation based on ray tracing was made by Johnson et al. (1963). Our
483 study also shows that the top of slopes is efficient at generating T waves be-
484 cause it allows for more energy to be redirected with low grazing angle. Let us
485 finally note that Figure 6 shows that this favored region exhibits relatively ho-
486 mogeneous energy but very different durations, suggesting a variable character
487 of T waves in that zone.
- 488 – The second region of interest is situated along the vertical of the slope, or along
489 a direction slightly oriented leftward (near the solid line in Figure 6). It is in this
490 region that we carried out the parametric study on the influence of the slope
491 presented in the previous section. This area allows for a maximum amount of
492 energy to be reflected on the slope. Our numerical simulations predict high
493 amplitude and rather short duration T waves there.

⁵ One could also think about a diffraction phenomenon on the sharp edges of the slope. Although we do observe this phenomenon in our simulations, the diffracted signals have negligible amplitude compared to the reflected ones

494 – To a lesser extent, a third favored area is observed in Figure 6. It approximately
495 follows a line originating at the top of the slope and oriented at 75° with respect
496 to the vertical (the dotted line in Figure 6). The energy emitted from a source
497 in this region and reflected off the slope, although weaker, has a small grazing
498 angle. More importantly, earthquakes located in this area are optimal for the
499 generation of energy that propagates between the shelf and the sea surface. Due
500 to the successive reflections on the shelf, these T waves have a long duration.

501 As an illustration, two signals of comparable energy but of different duration (ratio
502 of 1/3) are shown in Figure 7 (top). They have been recorded at range $L + d$ (see
503 Figure 1) in the middle of the water layer from a source either at the blue circle
504 or at the green square shown in Figure 6.

505 Earthquake magnitude and T-wave energy are known to be weakly correlated
506 (see e.g. Okal, 2007). The main explanation for this relates to the frequency band
507 used in estimating earthquake magnitude (anywhere from 1 Hz to 0.01 Hz or less
508 for CMT inversions), much less than the frequencies involved in T phases (typically
509 2 to 10 Hz). Note that the existence of favoured regions for T-wave generation may
510 reinforce this discrepancy.

511 Additionally, if the rupture zone crosses several areas with different transmis-
512 sion potentials, one can imagine that only some favored parts of the rupture, but
513 not necessarily the most energetic, will effectively contribute to the T wave, which
514 makes the phenomenon even more complex. It is also interesting to remark that
515 for the case studied we do not observe any clear trend between source depth and
516 signal duration for downslope generated T waves. However, T-waves generated at
517 the right of the line passing from the slope and oriented at an angle of 45° with
518 respect to the vertical (dashed line in Figure 6) tend to be of shorter duration.
519 If onset time and duration evolve similarly (which is not necessarily true), this
520 observation differs from the observations of Williams et al. (2006), who reported
521 a surprising correlation between rise time and water depth above the event. This

522 could suggest that the T waves observed by Williams et al. (2006) were generated
523 by scattering rather than by downslope conversion.

524 6 Conclusions and future work

525 In this paper, new observations have been made using parametric numerical sim-
526 ulations. We have quantified the importance of seabed slope, seabed seismic prop-
527 erties, velocity profile in the ocean and source position in the generation of a
528 two-dimensional downslope converted T wave. T-wave energy has been identified
529 as particularly sensitive to the slope of the seabed, which is seen as the most im-
530 portant parameter, then to seismic velocities in the seabed, and finally to source
531 position. For the quantities studied in this paper the SOFAR channel does not
532 seem to play a significant role at least in this frequency band (2-10 Hz) and for
533 short distances between epicenter and receivers (85 km). Our experience tells us
534 that this will remain true for distances up to several hundred kilometers. However,
535 this will probably no longer be the case for long propagation distances (> 5000
536 km). Low density sediments are seen to favor the generation of T waves by downs-
537 lope conversion, as predicted by ray theory. For a given source position, downslope
538 energy transmission is maximum for typically two slope angles. As more energy
539 can be potentially converted at these slopes, we suggest that this can bias local-
540 ization algorithms towards them, and not necessarily towards steepest slopes, as
541 often supposed, despite the fact that it is the most common situation.

542 Energy and duration maps have been constructed in order to analyze the in-
543 fluence of the source position for a given slope. This study showed that large vari-
544 ations in energy and duration can exist between T phases generated by sources
545 located at different positions with respect to the slope. The complex patterns
546 observed may partly account for the documented poor correlation between earth-
547 quake magnitude and T-wave energy (together with the different frequency bands
548 commonly used to calculate these quantities).

549 These maps also hint that T waves can be generated, by downslope conver-
550 sion, following earthquakes that occur beneath abyssal plains, but only above a
551 given depth depending on the distance to the slope. This observation could have
552 interesting implications and explain some of the exceptions to the rule "epicenters
553 at the lower end, and [...] seaward, of the continental slope are typically weak or
554 not received" (Johnson et al., 1967).

555 The above results illustrate how complex T-wave generation phenomena can
556 be. They show that the energy of these waves not only depends on the magnitude
557 of the earthquake but also -and in comparable proportions- on the velocity of the
558 sediments, on the position of the seismic event and on seabed bathymetry. Let us
559 note that the radiation pattern of the source could have a significant influence as
560 well, further increasing the complexity of the phenomenon, and would deserve a
561 study in its own right.

562 Our work suggests that due to the extreme complexity of T-wave conversion
563 and the limited availability of analytical models, earthquake localization based on
564 T waves will be difficult to improve with conventional methods. Nevertheless the
565 use of machine learning methods seems particularly promising in this context. The
566 current impressive growth in this field, which manages to deal with increasingly
567 complex problems, may probably create very significant advances in the use of T
568 waves for earthquake localization using T waves. (see for example Niu et al., 2017
569 in the context of ocean acoustic source localization).

570 A companion paper dealing with the upslope conversion/reflection of T waves
571 when reaching the shore will be published soon separately.

572 Acknowledgements D.K. would like to thank Jeroen Tromp for suggesting him to work on T
573 waves, a long time ago. We thank also Emmanuel Le Clezio and Eric Rosenkrantz for their
574 help in validating the reflection coefficients. We also thank Emile Okal and an anonymous
575 reviewer for their useful comments that improved the manuscript. The Ph.D. grant of Alexis
576 Bottero was awarded by ENS Cachan, France. This work was granted access to the French
577 HPC resources of CINES under allocation #A0020407165 and #A0030410305, both made by
578 GENCI, and of the Aix-Marseille Supercomputing Mesocenter under allocations #b025. We

579 gratefully acknowledge the support of NVIDIA Corporation with the donation of hardware for
580 this research through their Hardware Grant Request program.

581 References

- 582 Adams RD (1979) T-phase recordings at Rarotonga from underground nuclear
583 explosions. *Geophysical Journal of the Royal Astronomical Society* 58(2):361–
584 369, DOI 10.1111/j.1365-246X.1979.tb01030.x
- 585 Båth M (1954) A study of T phases recorded at the Kiruna seismograph station.
586 *Tellus* 6(1):63–72
- 587 Blackman DK, Nishimura CE, Orcutt JA (2000) Seismoacoustic recordings of a
588 spreading episode on the Mohns Ridge. *Journal of Geophysical Research: Solid*
589 *Earth* 105(B5):10961–10973
- 590 Boatwright J, Choy GL (1986) Teleseismic estimates of the energy radi-
591 ated by shallow earthquakes. *J Geophys Res* 91(B2):2095–2112, DOI
592 10.1029/JB091iB02p02095
- 593 Bohnenstiehl DR, Dziak RP, Matsumoto H, Lau TKA (2013) Underwater acoustic
594 records from the March 2009 eruption of Hunga Ha’apai-Hunga Tonga volcano
595 in the Kingdom of Tonga. *Journal of Volcanology and Geothermal Research*
596 249:12–24, DOI 10.1016/j.jvolgeores.2012.08.014
- 597 Bottero A, Cristini P, Komatitsch D, Asch M (2016) An axisymmetric time-
598 domain spectral-element method for full-wave simulations: Application to ocean
599 acoustics. *Journal of the Acoustical Society of America* 140(5):3520–3530, DOI
600 10.1121/1.4965964
- 601 Bottero A, Cristini P, Komatitsch D, Brissaud Q (2018) Broadband transmission
602 losses and time dispersion maps from time-domain numerical simulations in
603 ocean acoustics. *The Journal of the Acoustical Society of America* 144(3):EL222–
604 EL228
- 605 Carcione JM, Helle HB (2004) The physics and simulation of wave propagation at
606 the ocean bottom. *Geophysics* 69(3):825–839

- 607 Chapman NR, Marrett R (2006) The directionality of acoustic T-phase signals
608 from small magnitude submarine earthquakes. *Journal of the Acoustical Society*
609 *of America* 119(6):3669–3675, DOI 10.1121/1.2195073
- 610 Cowen JP, Baker ET, Embley RW (2004) Detection of and response to mid-
611 ocean ridge magmatic events: Implications for the subsurface biosphere. *The*
612 *Subseafloor Biosphere at Mid-Ocean Ridges* pp 227–243
- 613 Cristini P, Komatitsch D (2012) Some illustrative examples of the use of a spectral-
614 element method in ocean acoustics. *Journal of the Acoustical Society of America*
615 131(3):EL229–EL235, DOI 10.1121/1.3682459
- 616 De Groot-Hedlin C (2005) Estimation of the rupture length and velocity of the
617 Great Sumatra earthquake of dec 26, 2004 using hydroacoustic signals. *Geo-*
618 *physical Research Letters* 32(11):n/a–n/a, DOI 10.1029/2005GL022695, 111303
- 619 De Groot-Hedlin C, Orcutt JA (1999) Synthesis of earthquake-generated T-waves.
620 *Geophysical Research Letters* 26(9):1227–1230, DOI 10.1029/1999GL900205
- 621 De Groot-Hedlin C, Orcutt JA (2000) Detection of T-phases at island seismic
622 stations: Dependence on seafloor slope, seismic velocity and roughness. Tech.
623 rep., Scripps Institution Of Oceanography La Jolla CA
- 624 De Groot-Hedlin C, Orcutt JA (2001) *Monitoring the Comprehensive Nuclear-*
625 *Test-Ban-Treaty: Hydroacoustics*. Springer
- 626 De Groot-Hedlin C, Blackman D, Orcutt J (2004) The use of hydroacoustic phases
627 for the detection of oceanic events: Observations and numerical modeling. Tech.
628 rep., Scripps Institution Of Oceanography La Jolla CA
- 629 Delaney JR, Kelley DS, Lilley MD, Butterfield DA, Baross JA, Wilcock WSD,
630 Embley RW, Summit M (1998) The quantum event of oceanic crustal accretion:
631 Impacts of diking at mid-ocean ridges. *Science* 281(5374):222–230
- 632 Dietz RS, Sheehy MJ (1954) Transpacific detection of Myojin volcanic ex-
633 plosions by underwater sound. *GSA Bulletin* 65(10):941, DOI 10.1130/0016-
634 7606(1954)65[941:TDOMVE]2.0.CO;2

- 635 Duennebieer FK, Johnson RH (1967) T-phase sources and earthquake epicenters
636 in the Pacific basin. Tech. rep., Hawaii Institute Of Geophysics University of
637 Hawaii Honolulu
- 638 Dziak RP (2001) Empirical relationship of T-wave energy and fault parameters of
639 northeast Pacific ocean earthquakes. *Geophysical Research Letters* 28(13):2537–
640 2540, DOI 10.1029/2001GL012939
- 641 Dziak RP, Hammond SR, Fox CG (2011) A 20-year hydroacoustic time series of
642 seismic and volcanic events in the northeast Pacific ocean. *Oceanography* 24
- 643 Dziak RP, Bohnenstiehl DR, Smith DK (2012) Hydroacoustic monitoring of
644 oceanic spreading centers: Past, present, and future. *Oceanography* 25(1):116–
645 127
- 646 Evers LG, Snellen M (2015) Passive probing of the sound fixing and ranging chan-
647 nel with hydro-acoustic observations from ridge earthquakes. *Journal of the*
648 *Acoustical Society of America* 137(4):2124–2136
- 649 Ewing M, Press F, Worzel JL (1952) Further study of the T phase. *Bull seism Soc*
650 *Am* 42:37–51
- 651 Fichtner A (2010) Full Seismic Waveform Modelling and Inversion. *Advances in*
652 *Geophysical and Environmental Mechanics and Mathematics*, Springer-Verlag,
653 Berlin, Germany, 343 pages.
- 654 Fox CG, Dziak RP (1998) Hydroacoustic detection of volcanic activity on the
655 Gorda ridge, February-March 1996. *Deep Sea Research Part II: Topical Studies*
656 *in Oceanography* 45(12):2513–2530, DOI 10.1016/S0967-0645(98)00081-2
- 657 Fox CG, Dziak RP, Matsumoto H, Schreiner AE (1994) Potential for monitoring
658 low-level seismicity on the Juan de Fuca Ridge using military hydrophone arrays.
659 *Marine Technology Society Journal* 27(4):22–30
- 660 Fox CG, Radford WE, Dziak RP, Lau TK, Matsumoto H, Schreiner AE (1995)
661 Acoustic detection of a seafloor spreading episode on the Juan de Fuca ridge
662 using military hydrophone arrays. *Geophysical Research Letters* 22(2):131–134

- 663 Fox CG, Matsumoto H, Lau TKA (2001) Monitoring Pacific Ocean seismicity from
664 an autonomous hydrophone array. *Journal of Geophysical Research: Solid Earth*
665 106(B3):4183–4206
- 666 Frank SD, Collis JM, Odom RI (2015) Elastic parabolic equation solutions for
667 oceanic T-wave generation and propagation from deep seismic sources. *Journal*
668 *of the Acoustical Society of America* 137(6):3534–3543
- 669 Graeber FM, Piserchia PF (2004) Zones of T-wave excitation in the NE Indian
670 ocean mapped using variations in backazimuth over time obtained from multi-
671 channel correlation of IMS hydrophone triplet data. *Geophysical Journal Inter-*
672 *national* 158(1):239–256
- 673 Guilbert J, Vergoz J, Schissele E, Roueff A, Cansi Y (2005) Use of hydroacoustic
674 and seismic arrays to observe rupture propagation and source extent of the
675 Mw = 9.0 Sumatra earthquake. *Geophysical Research Letters* 32(15), DOI
676 10.1029/2005GL022966
- 677 Hammond SR, Walker DA (1991) Ridge event detection: T-phase signals from the
678 Juan de Fuca spreading center. *Marine Geophysical Researches* 13(4):331–348,
679 DOI 10.1007/BF00366282
- 680 Jamet G, Guennou C, Guillon L, Mazoyer C, Royer JY (2013) T-wave generation
681 and propagation: A comparison between data and spectral element modeling.
682 *Journal of the Acoustical Society of America* 134(4):3376–3385
- 683 Jensen FB, Kuperman W, Porter M, Schmidt H (2011) *Computational Ocean*
684 *Acoustics*, 2nd edn. Springer-Verlag, Berlin, Germany, 794 pages.
- 685 Johnson RH (1966) Routine location of T-phase sources in the Pacific. *Bulletin of*
686 *the Seismological Society of America* 56(1):109–118
- 687 Johnson RH, Northrop J (1966) A comparison of earthquake magnitude with T-
688 phase strength. *Bulletin of the Seismological Society of America* 56(1):119–124
- 689 Johnson RH, Northrop J, Eppley R (1963) Sources of Pacific T phases. *Journal of*
690 *Geophysical Research* 68(14):4251–4260, DOI 10.1029/JZ068i014p04251

- 691 Johnson RH, Norris RA, Duennebieer FK (1967) Abyssally generated T phases.
692 Tech. rep., Hawaii Institute Of Geophysics University of Hawaii Honolulu
- 693 Komatitsch D, Martin R (2007) An unsplit convolutional perfectly matched
694 layer improved at grazing incidence for the seismic wave equation. *Geophysics*
695 72(5):SM155–SM167
- 696 Komatitsch D, Tromp J (1999) Introduction to the spectral-element method for 3-
697 D seismic wave propagation. *Geophys J Int* 139(3):806–822, DOI 10.1046/j.1365-
698 246x.1999.00967.x
- 699 Kosuga M (2011) Localization of T-wave energy on land revealed by a dense seismic
700 network in japan. *Geophysical Journal International* 187(1):338–354
- 701 Koyanagi S, Aki K, Biswas N, Mayeda K (1995) Inferred attenuation from site
702 effect-corrected T phases recorded on the island of Hawaii. *Pure and Applied*
703 *Geophysics* 144(1):1–17
- 704 Lecoulant J, Guennou C, Guillon L, Royer JY (2019) Three-dimensional model-
705 ing of earthquake generated acoustic waves in the ocean in simplified config-
706 urations. *The Journal of the Acoustical Society of America* 146(3):2113–2123,
707 DOI 10.1121/1.5126009
- 708 Linehan SJD (1940) Earthquakes in the West Indian region. *Transactions Ameri-
709 can Geophysical Union* 21:229–232
- 710 Matsumoto H, Bohnenstiehl DR, Tournadre J, Dziak RP, Haxel JH, Lau TK,
711 Fowler M, Salo SA (2014) Antarctic icebergs: A significant natural ocean
712 sound source in the southern hemisphere. *Geochemistry, Geophysics, Geosys-
713 tems* 15(8):3448–3458
- 714 Metz D, Watts AB, Grevemeyer I, Rodgers M, Paulatto M (2016) Ultra-
715 long-range hydroacoustic observations of submarine volcanic activity at
716 Monowai, Kermadec Arc. *Geophysical Research Letters* 43(4):1529–1536, DOI
717 10.1002/2015GL067259
- 718 Munk WH (1974) Sound channel in an exponentially stratified ocean, with appli-
719 cation to SOFAR. *Journal of the Acoustical Society of America* 55(2):220–226

- 720 Niu H, Reeves E, Gerstoft P (2017) Source localization in an ocean waveguide
721 using supervised machine learning. *Journal of the Acoustical Society of America*
722 142(3):1176–1188, DOI 10.1121/1.5000165
- 723 Norris RA, Johnson RH (1969) Submarine volcanic eruptions recently located in
724 the pacific by SOFAR hydrophones. *Journal of Geophysical Research* 74(2):650–
725 664
- 726 Northrop J (1962) Evidence of dispersion in earthquake T phases. *Journal of Geo-*
727 *physical Research* 67(7):2823–2830, DOI 10.1029/JZ067i007p02823
- 728 Okal EA (2001) "Detached" deep earthquakes: Are they really? *Physics of the*
729 *Earth and Planetary Interiors* 127(1):109–143
- 730 Okal EA (2003) T waves from the 1998 Papua New Guinea earthquake and
731 its aftershocks: Timing the tsunamigenic slump. *Pure and Applied Geophysics*
732 160(10):1843–1863, DOI 10.1007/s00024-003-2409-x
- 733 Okal EA (2007) The generation of T waves by earthquakes. *Adv Geophys* 49:1–65
- 734 Okal EA, Talandier J (1997) T waves from the great 1994 Bolivian deep earthquake
735 in relation to channeling of S wave energy up the slab. *Journal of Geophysical*
736 *Research: Solid Earth* 102(B12):27421–27437, DOI 10.1029/97JB02718
- 737 Pan J, Dziewonski AM (2005) Comparison of mid-oceanic earthquake epicen-
738 tral differences of travel time, centroid locations, and those determined by
739 autonomous underwater hydrophone arrays. *Journal of Geophysical Research:*
740 *Solid Earth* 110(B7)
- 741 Peter D, Komatitsch D, Luo Y, Martin R, Le Goff N, Casarotti E, Le Loher P,
742 Magnoni F, Liu Q, Blitz C, Nissen-Meyer T, Basini P, Tromp J (2011) For-
743 ward and adjoint simulations of seismic wave propagation on fully unstruc-
744 tured hexahedral meshes. *Geophys J Int* 186(2):721–739, DOI 10.1111/j.1365-
745 246X.2011.05044.x
- 746 Rosenkrantz E, Bottero A, Komatitsch D, Monteiller V (2019) A flexible numer-
747 ical approach for non-destructive ultrasonic testing based on a time-domain
748 spectral-element method: Ultrasonic modeling of lamb waves in immersed de-

- 749 fective structures and of bulk waves in damaged anisotropic materials. *NDT &*
750 *E International* 101:72–86
- 751 Salzberg D (2008) A hydro-acoustic solution to the local tsunami warning problem.
752 In: AGU Fall Meeting Abstracts
- 753 Schreiner AE, Fox CG, Dziak RP (1995) Spectra and magnitudes of T-waves from
754 the 1993 earthquake swarm on the Juan de Fuca Ridge. *Geophysical Research*
755 *Letters* 22(2):139–142, DOI 10.1029/94GL01912
- 756 Shurbet DH (1955) Bermuda T phases with large continental paths. *Bulletin of*
757 *the Seismological Society of America* 45(1):23–35
- 758 Shurbet DH, Ewing M (1957) T phases at Bermuda and transformation of elastic
759 waves. *Bulletin of the Seismological Society of America* 47(3):251–262
- 760 Sukhovich A, Irisson JO, Perrot J, Nolet G (2014) Automatic recognition of T
761 and teleseismic P waves by statistical analysis of their spectra: An application
762 to continuous records of moored hydrophones. *Journal of Geophysical Research:*
763 *Solid Earth* 119(8):6469–6485
- 764 Talandier J, Okal EA (1987) Seismic detection of underwater volcanism: The ex-
765 ample of French Polynesia. *Pure and Applied Geophysics* 125(6):919–950
- 766 Talandier J, Okal EA (1998) On the mechanism of conversion of seismic waves to
767 and from T waves in the vicinity of island shores. *Bull seism Soc Am* 88(2):621–
768 632
- 769 Talandier J, Okal EA (2016) A new source discriminant based on frequency disper-
770 sion for hydroacoustic phases recorded by T-phase stations. *Geophysical Journal*
771 *International* 206(3):1784–1794, DOI 10.1093/gji/ggw249
- 772 Talandier J, Hyvernaud O, Reymond D, Okal EA (2006) Hydroacoustic signals
773 generated by parked and drifting icebergs in the southern indian and pacific
774 oceans. *Geophysical Journal International* 165(3):817–834
- 775 Tolstoy I, Ewing M (1950) The T phases of shallow-focus earthquakes. *Bull seism*
776 *Soc Am* 40:25–51

-
- 777 Tolstoy M, Bohnenstiehl DR (2005) Hydroacoustic constraints on the rupture
778 duration, length, and speed of the great Sumatra-Andaman earthquake. *Seis-*
779 *mological Research Letters* 76(4):419–425
- 780 Tolstoy M, Bohnenstiehl DR (2006) Hydroacoustic contributions to understand-
781 ing the December 26th 2004 great Sumatra-Andaman earthquake. *Surveys in*
782 *Geophysics* 27(6):633–646, DOI 10.1007/s10712-006-9003-6
- 783 Wadati K, Inouye W (1953) On the T phase of seismic waves observed in Japan.
784 *Proc Japan Acad* 29:47–54
- 785 Wilcock WSD, Stafford KM, Andrew RK, Odom RI (2014) Sounds in the ocean
786 at 1-100 Hz. *Annual review of marine science* 6:117–140
- 787 Williams CM, Stephen RA, Smith DK (2006) Hydroacoustic events located at
788 the intersection of the Atlantis (30°N) and Kane (23°40'N) transform faults
789 with the Mid-Atlantic ridge. *Geochemistry, Geophysics, Geosystems* 7(6):1–28,
790 DOI 10.1029/2005GC001127
- 791 Xie Z, Matzen R, Cristini P, Komatitsch D, Martin R (2016) A perfectly matched
792 layer for fluid-solid problems: Application to ocean-acoustics simulations with
793 solid ocean bottoms. *Journal of the Acoustical Society of America* 140(1):165–
794 175, DOI 10.1121/1.4954736

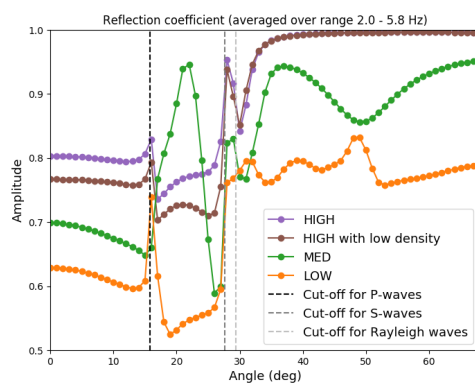
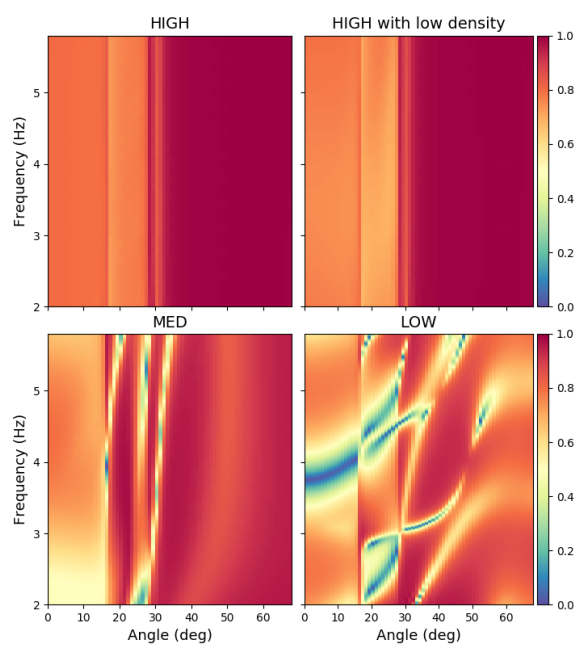
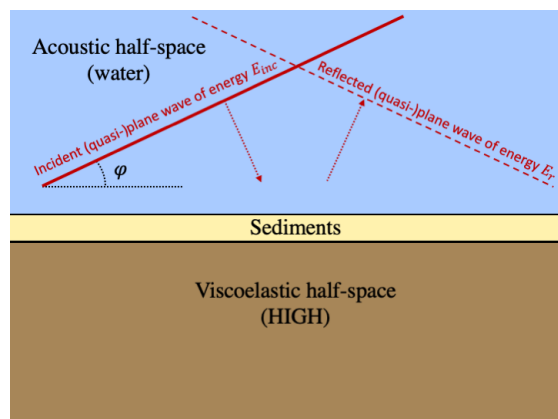


Fig. 5 Top: setting of the energy reflection coefficient shown below (E_{inc}/E_r). Middle: energy reflection coefficient for oceanic plane waves as a function of frequency and incidence angle φ (defined in the top sub-figure) at the water-sediments interface for the cases described in Table 1. The frequency range shown corresponds to the bandwidth of the source. Bottom: same but averaged over the frequencies shown.

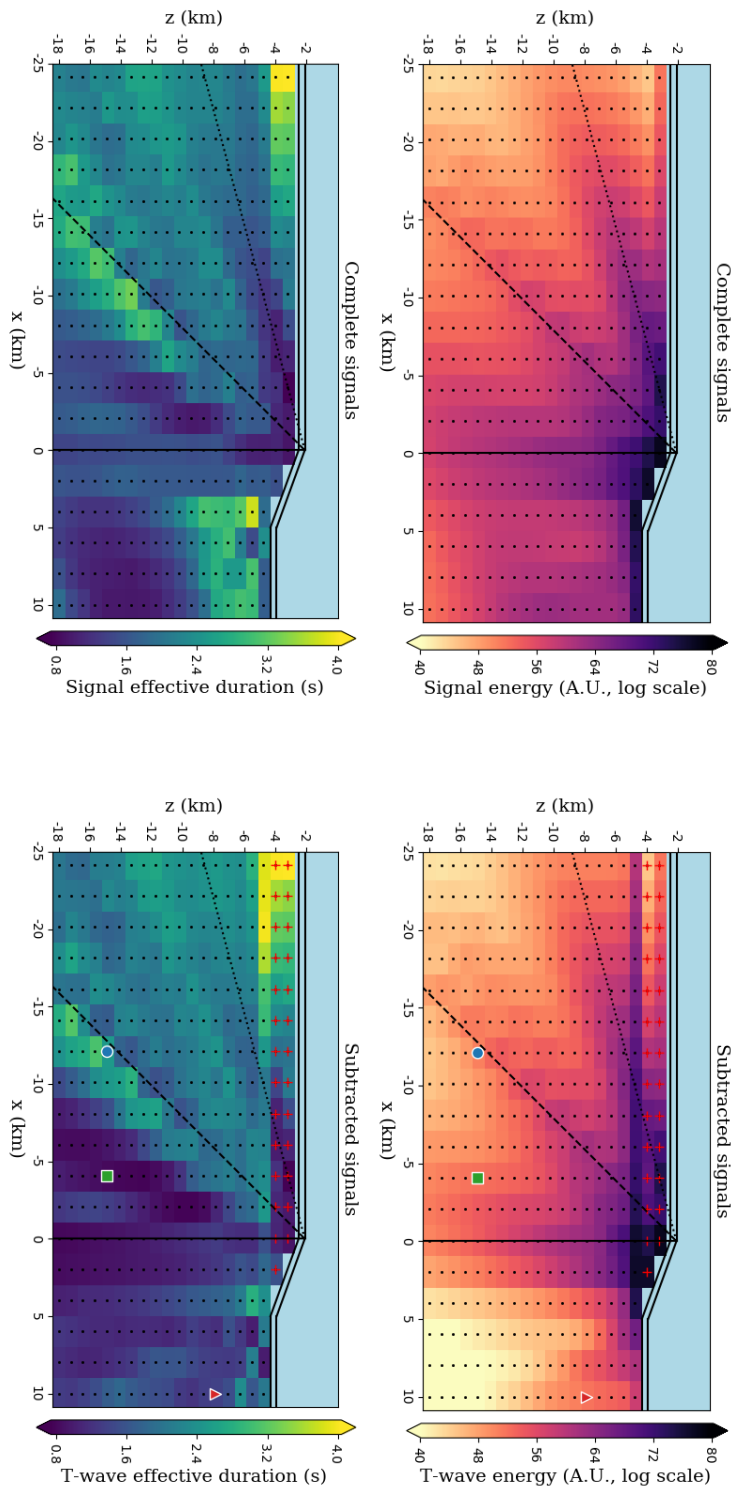


Fig. 6 This figure summarizes the energy (top, in arbitrary logarithmic unit) and effective duration (bottom, in seconds) of the signals recorded at a distance of 85 km from the top of the slope for different source positions represented as black dots or red crosses. On the right the body waves have been subtracted for the sources represented in black using the process described in the text. No subtraction has been made for the sources represented as red crosses nor for the pictures on the left. The blue circle, green square and red triangle indicate the locations at which the signals shown in Figure 7 (top) are recorded. The dashed line is tilted by an angle of 45° with respect to the vertical direction represented by the other solid line. The dotted line is tilted by an angle of 75° .

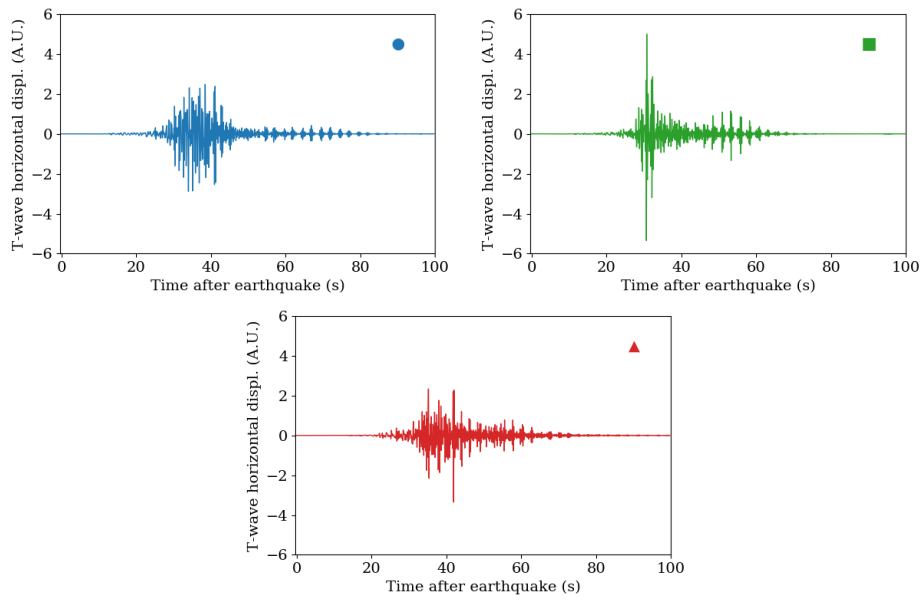


Fig. 7 T-wave horizontal displacement (after body wave subtraction) generated by the three earthquakes marked as a blue circle, a green square and a red triangle in Figure 6 respectively. The green signal is more impulsive compared to the blue and red ones.